Optical phase control for MMW sparse aperture upconversion imaging

Yuntao He (何云涛)[1*], Haiping Huang (黄海平)[1], Yuesong Jiang (江月松)[1], and Yuedong Zhang (张跃东)[2]

[1]*School of Electronic and Information Engineering, Beihang University, Beijing 100191, China*

[2]*Beijing Institute of Space Mechanics and Electricity, Beijing 100190, China*

[*]*Corresponding author: yuntaohe@buaa.edu.cn*

Received November 26, 2013; accepted March 5, 2014; posted online April 30, 2014

The random phase errors of the optical carriers are discussed and controlled for passive millimeter-wave sparse aperture (PMMW SA) upconversion imaging. A two-channel model is set up for analyzing characteristics of the phase errors, and an active optical control technique based on stochastic parallel gradient decent algorithm (SPGD controller) is proposed to calibrate the phase errors. To demonstrate the feasibility of the SPGD controller, simulations are performed and an experimental system with a two-channel fiber array is set up. Simulation and experiment results show that the SPGD controller can effectively and rapidly compensate the phase errors of the optical carrier, and the accuracy of the phase control is sufficient for imaging systems.

OCIS codes: 110.0110, 250.0250, 140.0140, 030.0030.

doi: 10.3788/COL201412.051101.

Passive millimeter wave (PMMW) imaging has shown significant potential over other technology capable of penetrating through low visibility conditions and obscurations caused by cloud, fog, smoke, sandstorms, and clothing. So PMMW imager could be widely used in homeland security, defense, and aviation safety[1,2]. However, the angular resolution of such an imager is limited by classical diffraction theory, $\Delta\theta = \lambda/D$, where D is the circular aperture diameter and λ is the free-space wavelength of the imager. Sparse aperture (SA) imaging techniques can obtain higher resolution by using many discrete apertures compared with the single large-aperture imaging technique. With regard to the traditional down-conversion imaging techniques utilizing a mixer to reduce the MMW signal frequency with electronic techniques, it is still suppressed by many technical problems, including high-sensitivity phase detectors, routing and a large array of complex cross-correlators, and interconnects for a real-time signal processing[3,4]. To circumvent these obstacles, several novel techniques of passive SA MMW imaging using optical upconversion techniques have been proposed[2−7]. Unlike conventional techniques, the optical upconversion technique realizes imaging by modulating the target MMW signals into optical sidebands and forming the target images on the optical domain. Although this technique shows significant potential for PMMW applications, a number of technical challenges must be overcome for such a system to be implemented[8,9]. Such challenges include: 1) New wide-band MMW signal processing techniques should be developed[10−12]; 2) The target signal must be routed from each node to a central processor without dispersion traveling through the fiber; 3) The optically upconverted signal experiences phase error induced by random variations in antenna positioning, atmospheric artifacts, stress-change in fiber, the fluctuations of the laser and so on. This letter focuses on a technique to ensure phase stability.

Minor variations in effective path length will cause dramatic changes in optical phase, making the coherent imaging techniques unfeasible[8]. In practical applications, it is necessary for us to restrict the change from fiber length to be less than $\lambda/10$ to get a high quality reconstructed image[3]. This would require the optical lengths to be controlled within 0.1 μm. Fortunately, the phase effects can be accounted for by actively compensating for induced changes in the optical path.

Several active phase control methods have been proposed to circumvent the phase effects in other kinds of optical system[12−19], such as heterodyne technique, multidither technique, redundant spacing calibration (RSC) and stochastic parallel gradient decent SPGD algorithm. This letter presents a technique called the optical carrier interference calibration by using SPGD algorithm to calibrate the phase errors in the fiber of an optical upconversion imaging system. To implement the algorithm, a program needs to execute after converting the phase errors to its related voltages.

Firstly, the sources of phase errors are analyzed with a two-channel phase errors model, and the calibration algorithm of SPGD is theoretically analyzed. Secondly, simulations are performed to verify the feasibility that the algorithm can calibrate the phase errors. In the end, the experimental validation of the algorithm is performed.

The schematic diagram of the optical upconversion imaging system is illustrated in Fig. 1. The target radiation signals received by the antenna array are modulated onto coherent optical carriers. After up-converting the signal onto sidebands, the optical signals are sequentially transmitted through polarization-maintaining (PM) fibers and a topology-maintained fiber array that matches the geometry of the antenna array at the fiber tails. Then the light is collimated and transmitted into

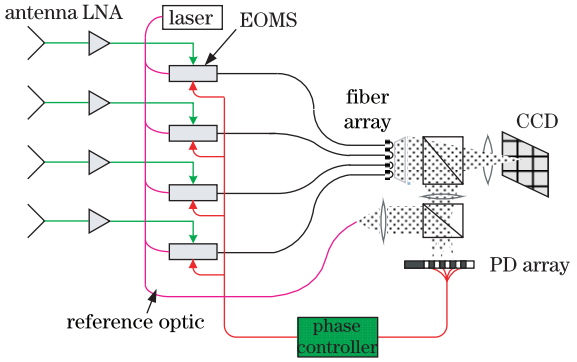

Fig. 1. Schematic diagram of the optical upconversion imaging system including active phase controller.

free space before forming images on the charge-coupled device (CCD).

The first order sidebands (FSBs) carry the amplitudes and the phases of incident signals from the target. The FSBs are separated from the carriers and higher order sidebands using a filter. All of the optical channels must be coherent and pass through a Fourier lens. After the optical FSB beams interference, the image is formed on the CCD plane. In order to measure the mutual coherence function, the signals from each antenna, which may be several meters apart, must be transported to a common location and then combined interferometrically. This can be achieved by supplying a light to each antenna from one narrow linewidth single-mode laser. The optical carriers are used to calibrate the phase errors.

Any phase difference between individual fibers will prevent image formation in this interferometric imaging system[3−21]. So it is necessary to compensate this error in the optical domain to maintain the phase of each individual imaging channel to the imaging plane. Herein, a real-time phase controller is adopted by comparing each optical beam of the fiber array to a reference one for the imaging system as shown in Fig. 1.

In order to implement the proposed calibration technique, we analyze the characteristics of the phase errors firstly. The field of a coherent and monochromatic beam from the laser can be written as

$$E_{\rm s} = A_{\rm o} \exp[j(wt + \phi], \tag{1}$$

where $A_{\rm o}$ is the amplitude, w is the angular frequency of the light, t represents time, j is the imaginary unit, and ϕ is the initial phase of the light.

Fiber fluctuations result in the time-variant random phase errors denoted by $\alpha(t)$, so the expression of an optical beam in the imaging plane can be described as

$$E = kE_{\rm s} \exp[j\alpha(t)] = A \exp[j(wt + \phi + \alpha(t))], \tag{2}$$

where k represents the amplitude attenuation factor, $A = kA_{\rm o}$, and E represents the input field of an optical combiner.

Here, the optical interference of the two beams is considered. In that case, the complex field expressions of the combiner inputs can be described as

$$E_1 = A \exp[j(wt + \phi_1 + \alpha_1(t))],$$
$$E_2 = A \exp[j(wt + \phi_2 + \alpha_2(t))].$$

And the interference of the two coherent beams can be expressed as

$$I = |E_1 + E_2| = 2A^2[1 + \cos(\Delta\phi + \Delta\alpha(t))], \tag{3}$$

where $\Delta\alpha(t) = \alpha_1(t) - \alpha_2(t)$ represents the phase difference between the optical beams of the outputs of combiner. We can calibrate this phase difference using the corresponded intensity.

It can be concluded that the phase errors in both FSBs and carriers have the same characteristics for they propagate through the same route/fiber. So the phase errors in FSBs which contain the MMW signals can be calibrated by add a phase shift in the propagation route. And the phase shift can be obtained by Eq. (3). Besides, the MMW power will have no influence on the carrier interferometric intensities, for it has no relationship with carrier and is much smaller than the optical carrier power[19,20].

Phase errors induced by minor fluctuations can be simultaneously apparent on carrier and FSBs[6,8,11,22]. Thus, the effects of fluctuations can be calibrated by accurately measuring the carrier phase errors and actively compensating by applying controlling voltages to electro-optic modulator (EOM). One practical way to derive the carrier phase errors is to use the interference intensity between optical carriers, namely carrier interference technique. Figure 2 shows an implementation of this method.

In order to achieve the closed-loop control system independently, the phase-modulated optical signal in the fiber array are collimated with the refractive lens array. These collimated beams then pass through a 50/50 beam splitter. One of the output beams pass through a filter to obtain the FSB sidebands for imaging, while the other with carrier beams is used for phase calibration. These carrier beams is overlapped by the reference light which passes through the beam expander and collimator. Then, the two kinds of beams will travel to a micro lens array and be focused on the photonic detectors (PD). By the PD array, we can get voltages of the PD outputs which are individually proportional to the interference intensities between each carrier and the reference light. Thereafter, the SPGD algorithm is adopted to calculate the controlling voltages based on these collected voltages, then the controlling voltages are fed into EOM. Each beam in the fiber array can be locked independently to the common reference light by using the above method.

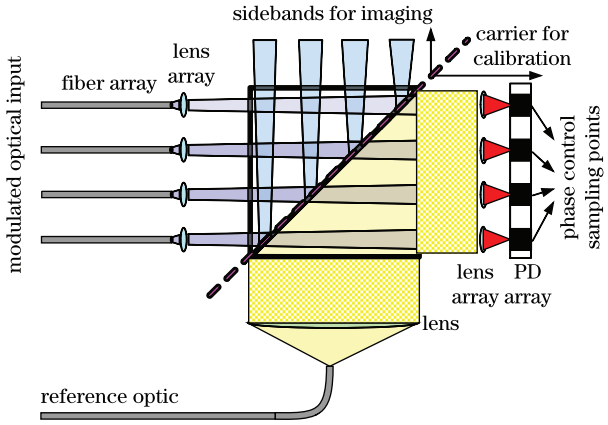

Fig. 2. Optical configuration used to lock optical carriers to reference beam.

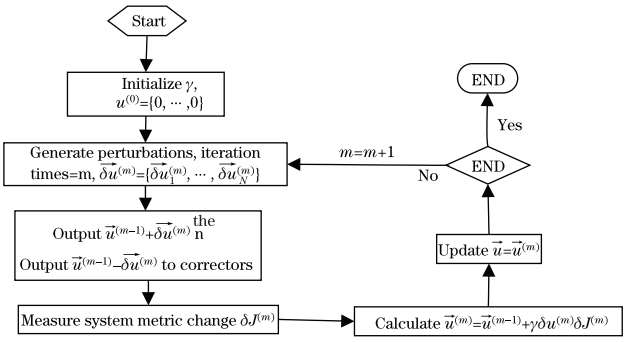

Fig. 3. Flow chart of SPGD algorithm.

As above mentioned, we know that the optical interference intensity between two optical beams is a cosine function of the phase difference. Although we get the output voltage of PD that is proportional to the interference intensity, it is still hard to precisely estimate the phase difference because it is a one-to-many relationship between the PD's voltage and its related phase difference.

The SPGD algorithm can circumvent this problem. Before implementing SPGD algorithm, it is necessary to preprocess the outputs of the PD array by a circuit. Thereafter, the processed voltages are used as the system performance metric J.

Phase errors can be eliminated by directly optimizing a measured metric J[17,23]. Here, m, N, τ, t, γ, δJ, s, $\overrightarrow{u}(t)$, $\delta_u J$, δu represent the iterations, the total channel number of the control loop, time constant, the real-time, the update factor, the metric change, the response factor of controlling voltage, the control vector, the first variation of the J, and the random perturbation, respectively. The subscript, n, represents the corresponding parameter for nth channel and the superscript, m, is the mth iteration time. The relationship between the partial derivative control phase, $\overrightarrow{u}(t)$, on time and the functional order about controlled phase variation has the following form:

$$\tau \frac{\partial \overrightarrow{u}(t)}{\partial t} = -\delta_u J. \tag{4}$$

The control vector $\overrightarrow{u}(t)$ should be produced by a limited number of correctors:

$$\overrightarrow{u}(t) = \sum_{n=1}^{N} s_n \times u_n(t). \tag{5}$$

From Eqs. (4) and (5), we can obtain ordinary differential equation:

$$\begin{aligned} \tau_n \frac{\mathrm{d}u_n(t)}{\mathrm{d}t} &= -\gamma \frac{\partial J(u_1(t), \cdots, u_N(t))}{\partial u_n(t)} \\ &= -\gamma J_n(u_1(t), \cdots, u_N(t)). \end{aligned} \tag{6}$$

From Eqs. (6), we have

$$\begin{aligned} \frac{\mathrm{d}J(t)}{\mathrm{d}t} &= \sum_{n=1}^{N} \frac{\partial J(t)}{\partial u_n(t)} \frac{\mathrm{d}u_n(t)}{\mathrm{d}t} \\ &= -\gamma \sum_{n=1}^{N} \left(\frac{\partial J}{\partial u_n(t)} \right)^2 \tau_n^{-1} \geqslant 0, (\text{if}\, \gamma < 0), \end{aligned} \tag{7}$$

where $J(t) = J(u_1(t), \cdots, u_N(t))$.

As described by Eq. (7), the system described by Eq. (6) is always stable near the extreme point. And the update factor γ is positive for J minimization or negative otherwise.

The discrete vision of Eq. (6) presented as

$$u_n^{(m+1)} = u_n^{(m)} - \gamma J_n'(u_1^{(m)}, \cdots, u_N^{(m)}). \tag{8}$$

The estimation, $J_n'(u_1^{(m)}, \cdots, u_N^{(m)})$, can be replaced by $\partial J^m \partial u_n^m$ in real-time applications and obtained by applying a small statistically independent random disturbance to the control parameter u_n^m, and the corresponding system performance change is ∂J^m[17,24]. Expressions of the system performance change and the updating control voltage are presented as

$$\delta J^m = J(\overrightarrow{u(t)}^{(m-1)} + \overrightarrow{\delta u}^{(m)}) - J(\overrightarrow{u(t)}^{(m-1)} + \overrightarrow{\delta u}^{(m)}), \tag{9}$$

$$u_n^{(m+1)} = u_n^{(m)} - \gamma \delta J^{(m)} \delta u^{(m)_n}, n = 1, \cdots, N. \tag{10}$$

In experiment, the implement steps of SPGD algorithm is shown in Fig. 3. Compared with other methods, SPGD is simpler to implement by programming and it can automatic search the global extreme point. Herein, the SPGD algorithm is firstly introduced to compensate the phase errors in the optical upconversion imager.

Characteristics of the PDs show that the output voltages are proportional to the injected optical intensities in a certain range of the spectrum. Thus, with a PD input of optical intensities described in Eq. (3), the output voltage of PD can be written as

$$V_{\mathrm{PD}} = l * [2A^2(1 + \cos(\Delta\alpha(t)))], \tag{11}$$

where l is the responsivity of the PD. As the$\Delta\alpha(t)$determines the changing part of PD, the voltage of PD can be expressed as $V_{\mathrm{PD}}^{'} = 0.5\cos(\Delta\alpha(t))$, where 0.5 is the amplitude.

By setting the frequency of phase errors to 50 Hz, the simulation results of the PD voltage is shown in Fig. 4 as a function of the active feedback frequency using SIMULINK.

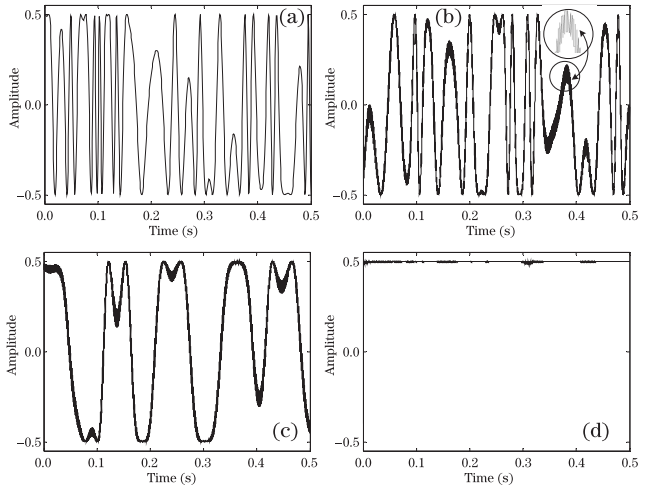

Fig. 4. Stability of simulation results as a function of the active feedback frequency while the frequency of the phase errors is 50 Hz. (a) No feedback loop; (b) 10-kHz feedback loop; (c) 50-kHz feedback loop; (c) 100-kHz feedback loop.

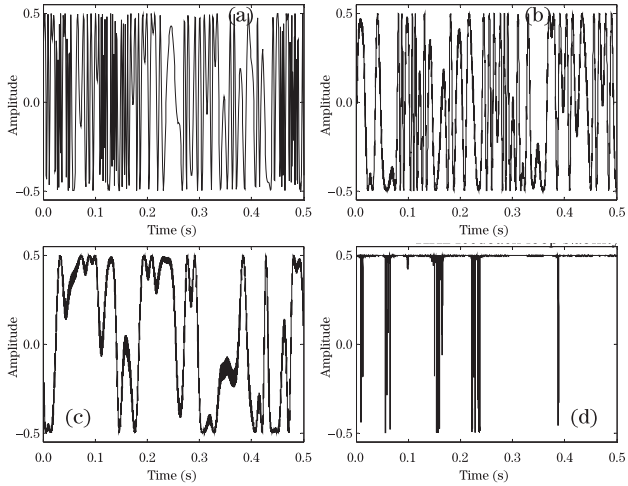

Fig. 5. Stability of simulation results as a function of the active feedback frequency. While the frequency of the phase errors is 100Hz. (a) No feedback loop; (b) 10-kHz feedback loop; (c) 50-kHz feedback loop; (c) 100-kHz feedback loop.

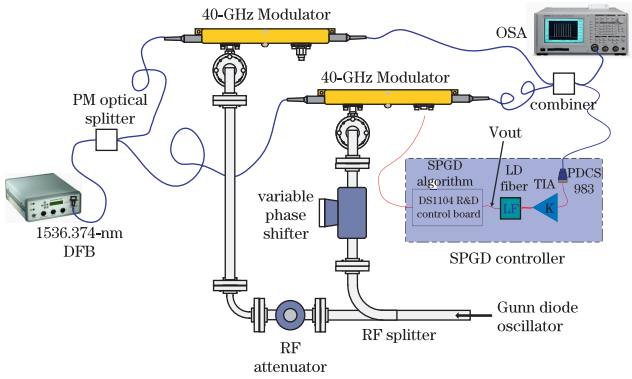

Fig. 6. Test setup to demonstrate optical upconversion of millimeter wave signals and active phase control calibration.

Figure 4(a) shows the output of PD without the feedback loop, and the value of this output is continuous random variable with a range from -0.5 to $+0.5$, which represents the phase errors changes from $-\pi$ to $+\pi$. When the active feedback frequency increases, the output of PD changes more and more slowly, shown in Figs. 4(d) and (c). From Fig. 4(d), we can see that the output of PD has a very minor fluctuations near the maximum point. It represents the phase errors fluctuate in a small range near minimum.

Increasing the frequency of phase errors to 100 Hz, we performed the simulation processes again. The corresponding results are shown in Fig. 5.

Compared with the output of PD shown in Fig. 4, the stability of each resulting output fluctuates more rapidly and its stability becomes worse with the same feedback frequency. The output of PD still cannot keep stable even though the feedback frequency runs at 100 kHz.

Table 1 lists RMS value of the output voltage of PD about the 8 subgraph.

From the simulation results, it can be concluded that: 1) the SPGD controller can effectively compensate the phase errors, and the stability of phase errors controlling depends greatly on the frequency of the feedback loop and the phase errors; 2) when the feedback frequency increases, the output voltage of PD becomes more and more stable near the maximum, and the RMS value is improved steadily; 3) Data listed in Table 2 show that it is need 1-kHz feedback frequency to compensate 1Hz phase errors. On the contrary, an increase in the frequency of phase errors will reduce the imaging performance and decrease the RMS. To improve the voltage stability of the PD, an effective method is to increase the feedback frequency.

To demonstrate the feasibility of the active phase control technique based on SPGD algorithm, we set up the experiment on a relatively stable experimental platform shown in Fig. 6.

The laser is power adjustable with center wavelength of 1536.500 nm and maximum output power of 31 mW. A 3-dB 1*2 splitter is connected to the output of the laser through PM fibers. Each output of the splitter is fed into a 40 Gb/s phase modulator from Covega (Model: Mach-40TM 027/066)[21]. The RF and the DC port of EOM are fed by the target signal and the phase controlling voltage generated by SPGD controller respectively. The phase shift has a linear relationship with the phase controlling voltage. The outputs of both modulators are combined with a 3-dB 2*2 combiner to form a Mach-Zehnder interferometer. One of the combiner outputs is fed into an optical spectrum analyzer (OSA) to obtain the optical spectrum while the other one is coupled to a PD. The output of PD is fed into a control board through the built-in A/D unit after passing through the trans-impedance amplifier and the low pass filter. The SPGD algorithm generates voltages for phase compensating, and a built-in D/A unit outputs the control voltages to the DC port of EOM for compensating the phase errors. The DA/AD and the SPGD algorithm functional units are integrated in a PCI control board, DS1104 from Dspace.

Table 1. Root Mean Square (RMS) Values Computed by 20000 Group Data

	0 kHz	10 kHz	50 kHz	100 kHz
50 Hz	0.3187	0.3476	0.4043	0.4821
100 Hz	0.3186	0.3225	0.3509	0.4684

Table 2. Phase Error Frequencies and the Related Feedback Frequencies

Noise Frequency/Hz	10	20	30	40	50	80	100
Feedback Frequency/kHz	12.5	21	30	40	50	81	102

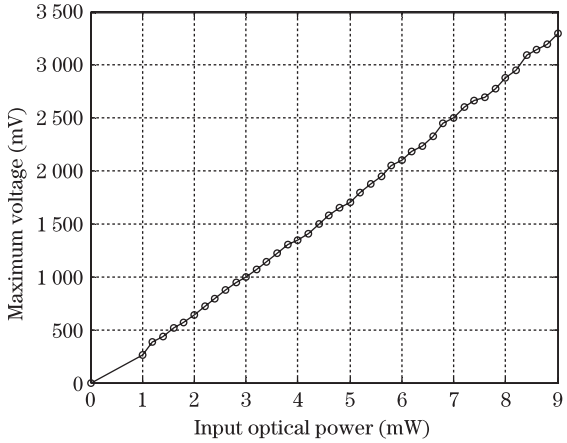

Fig. 7. Relationship between the maximum voltage output by PD and the corresponding input optical power.

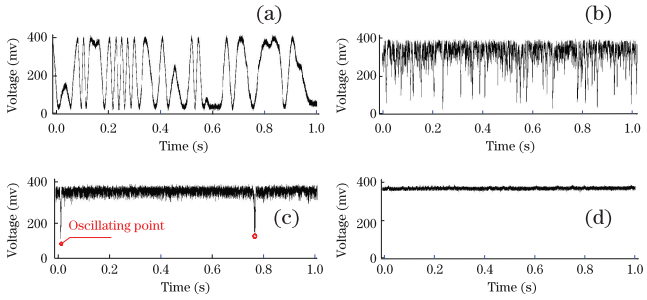

Fig. 8. Stability of the system performance metric (voltage output by LPF) as a function of the active feedback frequency. (a) No feedback loop showing the metric varying by more than 390 mV; (b) 1-kHz feedback loop showing improved stability but still some significant fluctuations; (c) 5-kHz; (d) 20-kHz feedback loops showing very minor the system performance metric fluctuations due to environmental conditions.

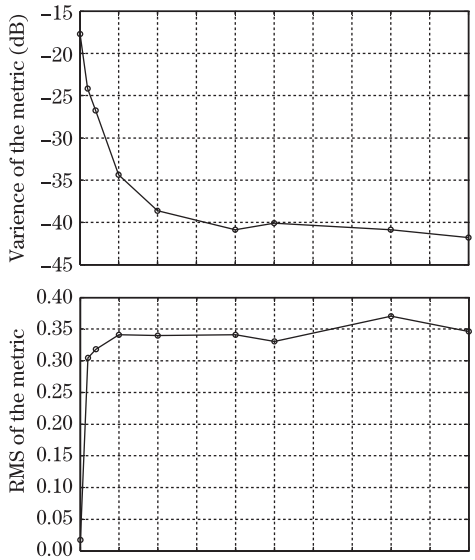

Fig. 9. (a) Variance as a function of the feedback frequency; (b) RMS as a function of the feedback frequency.

After setting up the experiment, we disconnect the connector marked by 'Vout' in Fig. 6 to confirm that the setup works properly. The maximum output voltage and the output power of the laser are recorded and shown in Fig. 7. It shows an approximately linear relationship between the maximum voltage and the power.

Then we connect the LPF to DS1104 and use an oscilloscope to obtain the output voltage of the LPF marked by 'Vout'.

Figure 8(a) shows that the voltage varies from 0−393 mV without feedback controlling. It represents the phase error between carriers changing from $-\pi$ to $+\pi$. Figure 8(b) shows the voltage of PD changes rapidly with a smaller range than that in Fig. 8(a) except for some isolated points during the observation time. And these points represent the significant phase fluctuations. Figure 8(c) shows that the fluctuations of voltage is much smaller than that in Fig. 8(b), also the number of isolated points reduces significantly with a feedback frequency of 5 kHz. The voltage shows a minor fluctuation of less than 38 mV near the maximum point. Increasing the feedback frequency to 20 kHz, the output voltage of LPF changes slightly near the peak and the points are non-existent, shown in Fig. 8(d). It represents that the phase errors due to environmental conditions is effectively compensated.

Herein, the RMS and the variance between the real-time voltage and the maximum point are adopted. Figure 9 shows the RMS and the variance as function of the feedback frequency.

The variance decrease rapidly while the feedback frequency increases from 0 to 5 kHz. Thereafter, the downward trend is much more gradual, as shown in Fig. 9(a). Finally, the variance changes very little near zero with a feedback frequency of 10 kHz. The trend of variation shows that the standard deviation will continue to fall until close to zero value. With regard to RMS shown in Fig. 9(b), it shows an opposite trend compared with the trend of variance. When the feedback frequency rises from 0 to 5 kHz, the value of RMS grows rapidly, and then the value rises moderately to the peak with minor fluctuations.

Figure 10(a) shows the optical spectrum at varions phase differences of EOM RF inputs from 0° to 180°. As can be seen from this figure, the measured powers in the optical sidebands are dependent on the phase introduced by the EOM RF inputs while the optical carrier has been suppressed effectively. In Fig. 10(b), it shows the peak power of the FSB (marked by rectangle and triangle) and the power of carrier (marked by circle). The changes of the carrier represent the fluctuations of the interference intensities between the optical carrier and the reference

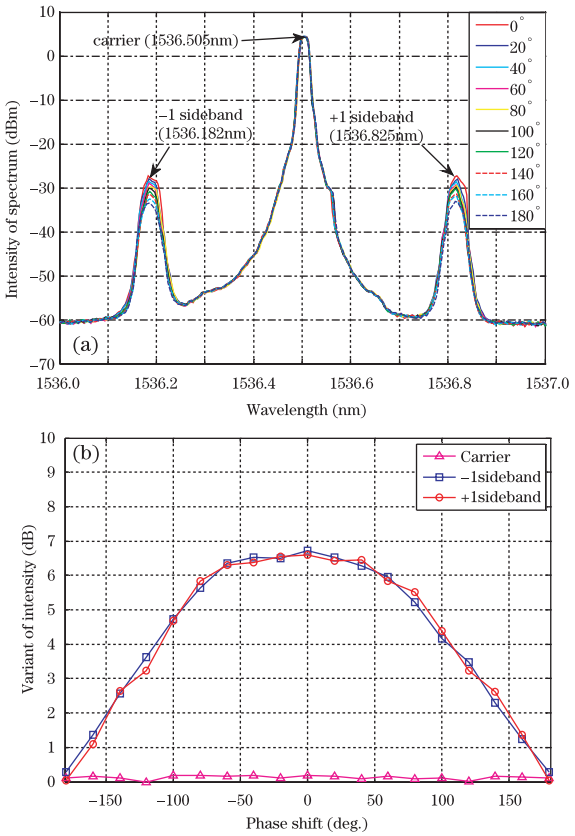

Fig. 10. (a) Optical spectra as the 40-GHz signal phase is adjusted from 0 to 180 degree taken with test setup; (b) change in amplitude (dB) of the carrier, ±1 optical signals taken from the data in Fig. 9.

beam. The fluctuations shown in Fig. 10(b) are less than 0.11 dBm,which represents a phase errors of 14.4^o at most. So the phase errors in the imaging system are corrected well through the SPGD controller. Similarly, the first sidebands intensity measured is a cosine function of the phase difference of EOM RF inputs. It means that the MMW signal is preserved very well when it travels through the fiber path with the feedback loop.

In conclusion, a feasible technique of the active phase control based on SPGD algorithm is proposed and applied for PMMW sparse aperture imaging. Simulations results show that the SPGD controller can efficiently compensate phase errors induced by variation of the fiber and other unpredictable factors. We also demonstrate the technical feasibilities of phase controlling of the two-channel fiber array using SPGD controller. Experimental results show that the phase fluctuations with the phase controlling are less than 14.4^0 that meets the accuracy requirement with a 20-kHz feedback frequency. Also the MMW signal preserves very well after passing through the fiber.

This work was supported by the National Natural Science Foundation of China under Grant No. 61101154.

References

1. L. Yujiri, M. Shoucri, and P. Moffa, IEEE Microwave Magazine **4,** 39 (2003).
2. A. N. Pergande, *PIE Security+ Defence. International Society for Optics and Photonics* 890006 (2013).
3. P. M. Blanchard, A. H. Greenaway, A. R. Harvey, and K. Webster, J. Lightwave Technol. **17,** 418(1999).
4. B. Braker and K. Wagner, Appl. Opt. **49,** E121 (2010).
5. C. A. Schuetz and D. W. Prather, *European Symposium on Optics and Photonics for Defence and Security. International Society for Optics and Photonics* (2004).
6. C. A. Schuetz, J. Murakowski, G. J. Schneider, and D. W. Prather, IEEE Trans. on Microwave Theory and Techniques **53,** 1732 (2005).
7. J. P. Wilson, C. A. Schuetz, T. E. Dillon, P. Yao, C. E. Harrity, and D.W. Prather, Appl. Opt. **51,** 4157 (2012).
8. C. A. Schuetz, R. D. Martin, I. Biswas, M. S. Mirotznik, S. Shi, G. J. Schneider, J. Murakowski, and D. W. Prather, Proc. SPIE **6211,** 62110G (2006).
9. R. Martin R, C. A. Schuetz, T. E. Dillon, C. hen C, J. Samluk, Jr. Stein, D. W. Prather and M. Mirotznik, *SPIE Defense, Security, and Sensing. International Society for Optics and Photonics* 730908 (2009).
10. E. R. Lopez, T. Lunn, K. Ghorbani, W. S. Rowe, and A. Mitchell, IEEE Trans. on Antennas and Propagation **57,** 3688 (2009).
11. A. A. Savchenkov, W. Liang, A. B. Matsko, V. S. Ilchenko, D. Seidel and L. Maleki, Opt. Lett. **34,** 1300 (2009).
12. S. J. Augst, T. Y. Fan, and A. Sanchez, Opt. Lett. **29,** 474 (2004).
13. H. Cui, W. Liao, N. Dai, and X. Cheng, Chin. Opt. Lett. **10,** 031201 (2012).
14. T. M. Shay, V. Benham, J. T. Baker, B. Ward, A. D. Sanchez, A. M. Culpepper, D. Pilkington, J. Spring, D. J. Nelson, and C. A. Lu, Opt. Express **14,** 12015 (2006).
15. B. Bennaï L. Lombard, V. Jolivet, C. Delezoide, E. Pourtal, P. Bourdon, G. Canat, O. Vasseur and Y. Jaouën, Fiber Int. Opt. **27,** 355 (2008).
16. A. Lannes and É. Anterrieu, J. Opt. Sci. Am. A, **16,** 2866 (1999).
17. M. A. Vorontsov, G. W. Carhart, M. Cohen, and G. Cauwenberghs, J. Opt. Sci. Am. A **17,** 1440(2000).
18. L. Liu and M. A. Vorontsov, *Optics & Photonics 2005 International Society for Optics and Photonics* 58950P (2005).
19. L. Jin and Z. Feng, Chin. Opt. Lett. **11,** 050201 (2013).
20. T. E. Dillon, C. A. Schuetz, R. D. Martin, S. Shi, D. G. Mackrides, and D. W. Prather, *Security+Defence. International Society for Optics and Photonics* (2010).
21. Y. He, Y. Jiang, Y. Zhang, and G. Fan, Chin. Opt. Lett. **8,** 162 (2010).
22. W. Zhang, X. Feng, W. Zhang, and X. Liu, Chin. Opt. Lett. **7,** 188 (2009).
23. M. H. Cohen, M. A. Vorontsov, G. W. Carhart and G. Cauwenberghs, *Remote Sensing. International Society for Optics and Photonics* 176 (1999).
24. M. A. Vorontsov and V. P. Sivokon, J. Opt. Sci. Am. A **15,** 2745 (1998).